

## 3-D Numerical Calculation of the Local Entropy Generation Rates in a Radial Compressor Stage

C. L. Iandoli<sup>†</sup>, E. Sciubba<sup>\*</sup>

Department of Mechanical Engineering,  
University of Rome 1 "La Sapienza"  
Via Eudossiana 18 – 00184 Rome, Italy  
E-mail: enrico.sciubba@uniroma1.it

### Abstract

The flow field in a low- $n_s$  radial compressor stage is computed by means of a LES simulation performed with a commercial CFD package. Radial and tangential secondary flows are identified both in the rotor and in the diffuser. In the latter, a regime of transient stall with a blockage region oscillating between the two sidewalls is observed. Rotor secondary flows influence the diffuser regime, and some of the diffuser instabilities seem to be phase-locked to some of the unsteady large flow structures detectable in the rotor. The entropy generation rate is computed locally, to assess if and where the design could be improved. Our results confirm that entropy generation maps (both in space and time) provide designers with detailed and unequivocal information about the causes of the intrinsic flow irreversibilities.

*Keywords: radial compressors, turbomachinery, CFD, flow entropy*

### 1. Introduction

The goal of this paper is to perform an entropy generation calculation on a radial compressor stage and show that the resulting "entropic maps" provide designers with additional useful information and help them conceive design improvements. The total entropy generation rate through the passage,  $\Delta S = dS/dt = d(s_2 - s_1)/dt$  (which is used in the calculation of the cascade efficiency, for instance), cannot directly reflect the specific local features of the flow that are necessary for its phenomenological interpretation, because it only provides the "control volume" view. It is, however, possible to express the irreversible entropy generation in terms of *local* flow quantities (see for instance Bejan (1982) and Sciubba (1994)): in the absence of phase changes and chemical reactions, the two dissipative mechanisms in viscous flow are the strain-originated dissipation  $\nu\Phi$  and the thermal dissipation  $k\nabla^2 T$ , which correspond to a "viscous" ( $\dot{s}_v$ ) and a "thermal" ( $\dot{s}_t$ ) entropy generation respectively. Thus, we can write:

$$\frac{ds}{dt} = \dot{s} = \dot{s}_v + \dot{s}_t = \mu \frac{\Phi}{T} + k \frac{\nabla^2 T}{T^2} \quad (1)$$

Notice that the entropy generation rate expressed by equation (1) is calculated per unit

volume ( $W/m^3C$ ), because this is more convenient from a computational point of view. Designers can use this steady state entropy balance in three ways:

- 1) Since  $\Phi = \Phi(u_{i,i}^2)$ , and it is relatively straightforward to conceptually link the shape of the blade profile with the local velocity gradients, maps of  $\dot{s}_v$  may be directly used as a design guide;
- 2) Similarly, since thermal gradients can be "controlled" either by blade cooling or by modifying wake mixing, maps of  $\dot{s}_t$  directly provide useful design information;
- 3) The global stage effectiveness is of course a function of  $dS/dt$ ; but this global entropy generation rate may also be computed as the volume integral of  $(ds/dt)_{dx dy dz} = (\dot{s}_v + \dot{s}_t)_{dx dy dz}$  over the entire flow domain, i.e. as the volume-weighted sum of the individual cell entropy generation rates over the  $N$  cells used in the geometric approximation of the real flow passage.

A possible procedure for "optimizing" a design by means of an entropy generation analysis may then be the following:

\*Author to whom correspondence should be addressed

<sup>†</sup>. Present address: Institute for Energy and Process Engineering, NTNU, Trondheim, Norway

1) Compute the flow details in the passage. It is mandatory that a viscous and turbulent model be used, and that the mesh resolution be high enough to capture the largest possible detail of the dissipative scales;

2) Extract the necessary information (local first derivatives  $u_{i,i}$  and  $T_i$ ) and display the maps of  $\dot{s}_v$  and  $\dot{s}_t$ ;

3) Integrate  $\dot{s}_v + \dot{s}_t$  over the entire flow domain to obtain  $dS/dt$ ;

4) Modify the design as suggested by a critical inspection of the local entropy generation maps;

5) Repeat the computation, and iterate until a feasible and acceptable “minimum” of  $dS/dt$  is reached.

It is apparent that the above is not a proper optimization, but rather a heuristic design approach, i.e. a (thermodynamically sound) trial-and-error procedure. Still, the amount of phenomenological information contained in the local entropy generation maps is so high that convergence towards a better design is almost guaranteed. As discussed in Bejan (1982), Iandoli (2000), Iandoli and Sciubba (2000) and Sciubba (2005), it is possible to derive an exact formula for both the viscous and the thermal components of the local entropy generation rates. In Cartesian notation, the expressions are as follow:

$$\dot{s}_v = \frac{\mu}{T} \left\{ \begin{array}{l} 2 \left[ \left( \frac{\partial u}{\partial x} \right)^2 + \left( \frac{\partial v}{\partial y} \right)^2 + \left( \frac{\partial w}{\partial z} \right)^2 \right] \\ + \left( \frac{\partial u}{\partial z} + \frac{\partial w}{\partial x} \right)^2 + \left( \frac{\partial u}{\partial y} + \frac{\partial v}{\partial x} \right)^2 \\ + \left( \frac{\partial v}{\partial z} + \frac{\partial w}{\partial y} \right)^2 \end{array} \right\} \quad (2)$$

$$\dot{s}_t = \frac{k}{T^2} \left[ \left( \frac{\partial T}{\partial x} \right)^2 + \left( \frac{\partial T}{\partial y} \right)^2 + \left( \frac{\partial T}{\partial z} \right)^2 \right] \quad (3)$$

To access this “entropic” information, it is therefore necessary to have a sufficiently detailed and precise representation of the local flow field, which in turbomachines is strongly dependent on the interaction between rotor and stator blades (Dawes 1995, Krain 1981, Reanu 1967). To reduce the computational intensity of the design task, numerical analyses are often performed on each one of the two cascades separately, neglecting unsteady effects induced by this interaction. This coupling must, though, be taken into account if the design must be truly optimized, and this can be done in different ways: the most popular at present, though still somewhat computationally expensive, is the use

of sliding meshes (Shum and Cumptsy, 2000). In this method, the domain is split into two parts in relative motion with respect to each other, and the flow quantities are computed using two different sets of equations in the two domains. The necessary coupling is obtained by proper interpolation in a “buffer domain” between the moving and the stationary parts. This explicit, mathematical coupling mimics the physical coupling, and provides the designer with useful information on the “real” flow field. But for turbulent flows, a significant portion of the physical phenomenology is hidden by a purely numerical interaction originated by the type of averaging employed at the sliding interface: without delving into this issue here, and referring the reader to Petters and Sleiman (2000) for a detailed treatment, we may say that the use of sliding meshes introduces a filtering effect on the upstream turbulence, thus preventing an exact assessment of the effects of the turbulent characteristics of the incoming flow field on the downstream cascade. Another problem, of an entirely different kind, is that in real machines the blade numbers of stator and rotor are usually prime with respect to each other, to avoid acoustic coupling. This requires an approximation in the definition of the computational domain, because the only way to reproduce the correct interaction would be that of simulating the entire stage and not only one blade passage. The commonly adopted fix is to assume that the number of blades of the two components is either the same or an integer multiple of each other: obviously, this leads to an incorrect radial periodicity either on the rotor or on the stator. The effect of this approximation, when applied to the numerical simulation of the flow field in a radial compressor, is that the calculated frequency of the pressure waves induced by the rotor on the stator is by force different from the real one. Since the rotor outlet pressure profile is far from being constant (Stein and Rautenberg, 1988), the stator will be subjected to pressure waves whose frequencies depend on the angular speed and the *numerical* (as opposed to the real) number of blades.

In this work, a different approach has been used: the rotor and the stator fields have been computed separately. The rotor flow field has been simulated first, with sufficient accuracy and detail so that relatively fine secondary flow effects, such as the influence of the slip factor and outlet pressure profile (Iandoli, 2000a,b), might be detected and quantified. A Fourier analysis of the outlet pressure was then performed and one “dominating” frequency was identified, which was selected to be the inlet boundary condition for the stator (diffuser). The results of this latter simulation show that many secondary flow effects in the diffuser can be observed without using the sliding mesh approach. In particular, a regime of transient stall

with a blockage region oscillating between the sidewalls has been observed. The method has its shortcomings: first of all, more than one frequency ought to be included to characterize the flow incoming into the diffuser. While there is no theoretical difficulty in doing this, the inclusion of higher frequencies requires finer statoric meshes, and makes the interpretation of the results more complicated. The second shortcoming is a conceptual one: since the rotor flow has been computed “in isolation”, i.e., with an assumed “downstream outflow condition”, the entire calculation ought to be iterated once the statoric flow field is known, to modify the rotor outlet conditions. This would be taxing in terms of computational intensity and has not been done here.

The final flow field (see *Figures 3, 4 and 5* below) has been validated by comparison to the available published data, and has been used to compute the entropy generation rate throughout the domain. As stated in our previous work (Iandoli, 2000a,b; Natalini and Sciubba, 1999; Sciubba, 1994), local entropy generation maps, especially if computed separately for their viscous and thermal contributions, provide substantial additional information about the flow regime and can be used directly to identify possible design changes.

## 2. Rotoric Flow Simulation

The rotor (*Figures 1 and 2*) has a purely axial inlet and 17 single-curvature blades. The flow is entirely 3-D, fully turbulent, and non-uniform in all three directions (axial, radial and tangential). A summary of the available design data is reported in TABLE I.

The computational domain does not include the inlet section, and the flow is assumed to possess a purely radial mean velocity when it impinges on the rotoric blades. This choice is justified by considering that the main objective of the simulation was to obtain reasonable pressure outlet profiles to be used in the stator simulation. These profiles are rather insensitive (within limits) to the presence of a small amount of inlet tangential velocity, but are instead strongly affected by the outlet boundary conditions. This latter influence was reduced by adding a 25 mm annulus at the outlet. At the end of this section a given constant outlet boundary conditions. This latter influence was reduced by adding a 25 mm annulus at the outlet. At the end of this section a given constant pressure was imposed. Annuli with different lengths were tested to determine a distance from the rotor outlet sufficient to ensure negligible effects on the pressure profiles at the rotor outlet.

The local irreversible entropy generation rates are calculated directly from local velocity and temperature values. Following the general

procedure outlined in previous works (Sciubba, 1994; Natalini and Sciubba, 1999), the entropy generation rate was split into its thermal and viscous contributions, and used to locate areas of relatively high losses. For this component the entropy production due to viscosity is the main dissipative effect, while the thermal contribution is almost negligible. Their maps are shown in *Figures 6 and 7*: notice that, since the rotor pressure ratio (*Figure 5*) is small, and the fluid is accelerated for the most portion of the channel (*Figure 4*), large velocity gradients are detectable at each radial section (*Figure 3*). Therefore, viscous dissipation is mainly located in the boundary layers (on the blades and both at hub and tip), though a small contribution is also provided by the wake region and the mid-channel region affected by the deceleration.

A global integration of the entropy generation rate is used to calculate the rotor II law efficiency. The lost work is the sum of the viscous and thermal entropy generation rates, equal here to  $s_{\text{thermal}}=0.00049$  W/K and  $s_{\text{viscous}}=0.076$  W/K. The II law efficiency is given by:

$$\eta_s = \frac{1}{1 + \frac{T_0 \Delta s}{h_{2,\text{ideal}} - h_1}} = 97\% \quad (4)$$

The result obtained using the II law approach is consistent with the value of the adiabatic efficiency derived above, and confirms that the component cannot be much improved. It is interesting to remark that the rotor object of the present simulation is of relatively simple construction: in particular, the trailing edge is realized by simply cutting the blades and the absence of splitting blades produces a rather poor

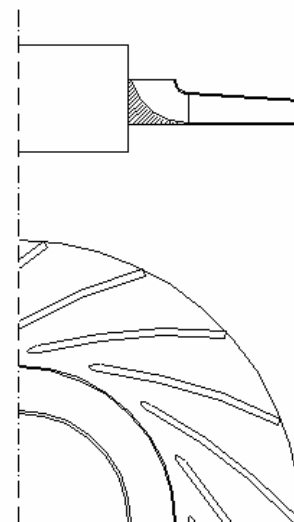


*Figure 1. Rotor geometry.*

TABLE I: THERMO-FLUID DYNAMIC DATA FOR THE ROTOR

Quantity	Symbol	Value
Mass flow rate	$\dot{m}$	1 kg/s
Rotor design angular velocity	$\omega$	1030 rad/s
Specific speed	$n_s$	0.39
Specific diameter	$d_s$	5.86
Number of rotor blades	$Z_r$	17
Inlet pressure	$p_1$	101325 Pa
Inlet temperature	$T_1$	298 K
Degree of reaction	$R_p$	0.6
Inlet radius	$r_1$	0.12 m
Outlet radius	$r_2$	0.2 m
Inlet blade height	$b_1$	0.016 m
Outlet blade span	$b_2$	0.015m
Blade thickness	$T$	0.005 m

pressure recovery. Nevertheless, our analysis does not justify any change in the wheel design based on an objective function consisting of the rotor efficiency.

### 3. Statoric Flow Simulation

The stator, produced by GE-Nuovo Pignone, consists of 27 passages, a section of the whole stage is reported in *Figure 2*. Both 2-D and 3-D simulations have been performed.

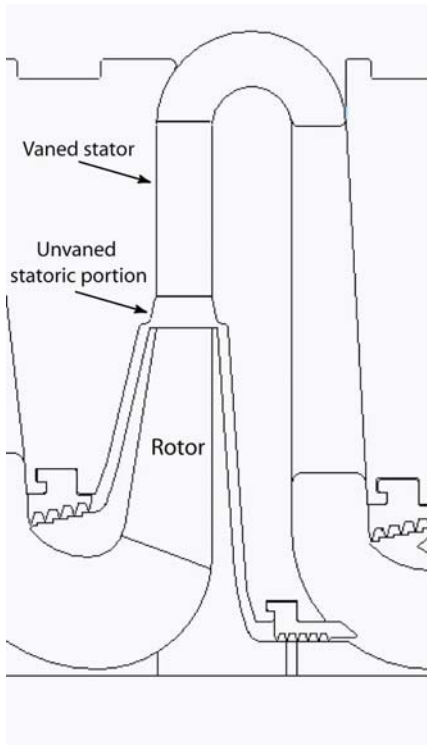


Figure 2. Section of the whole stage

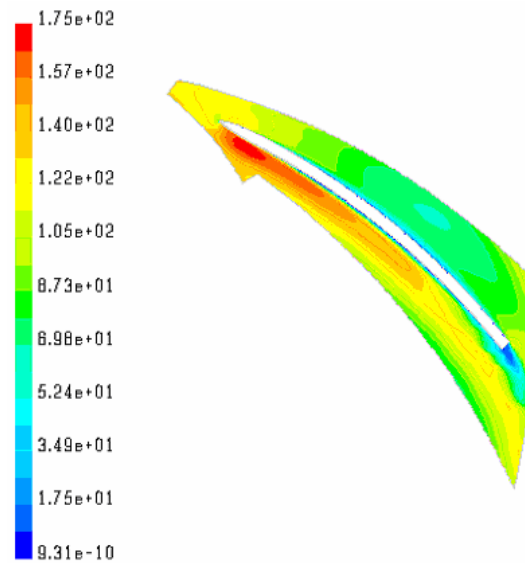


Figure 3. Velocity [m/s] contours at mid span

The computational 3-D grid consists of 500,000 hexahedral elements and is unstructured everywhere in the computational domain except in the boundary layers, where it consists of 10 layers. The thickness of the first of these layers determines the value of  $y^+$ , and since an LES turbulence model is used (Umlauf and Burchard, 2005),  $y^+$  must remain below 10. This requires a first row minimum thickness of 26  $\mu\text{m}$ . Thirty layers span the channel height from root to tip, with each surface divided into 17,000 quadrangular elements. In order to capture the fine details of the effects of both boundary layers

and wake, the grid has been adapted on the basis of the  $y^+$  and of the turbulent viscosity. The adaptation increased the total number of elements of about 10%.

The blade surface is treated as an adiabatic wall (no heat flux), while the static pressure is fixed at the outlet. As mentioned in Section 1, an unsteady total pressure has been imposed on the inlet surface. Both the steady and unsteady parts of this pressure have been computed on the basis of a Fourier analysis of the outlet pressure of the compressor rotor:

$$p_{\text{tot}}(t) = 175000 + 20000 \times \text{ABS}[\sin(17 \cdot (\theta - 1466 \cdot t))] \quad (5)$$

It can be easily seen that the pressure varies in time with a frequency proportional to both the speed of revolution of the rotor (1466 rad/s) and the number of rotor blades (17).

TABLE II – BOUNDARY CONDITIONS IMPOSED IN THE STATORIC SIMULATION.

Inlet	Outlet
$p_{\text{tot}} = f(t)$	$p_{\text{stat}} = 182430 \text{ Pa}$
$T_{\text{tot}} = 391 \text{ K}$	$T_{\text{tot,backflow}} = 391 \text{ K}$
$p_{\text{stat}} = 138000 \text{ Pa}$	

The total temperature is specified at the inlet surface, and it is assumed to be constant and equal to 391 K. TABLE II displays a summary of the imposed boundary conditions. The analysis of secondary flow phenomena demands for good modelling accuracy, and this suggested the use of a LES turbulence model. The simulation was unsteady and the time step used was proportional to the blade passage time: this is necessary to ensure that the unavoidable time-filtering (proportional to the time step) is sufficiently smaller than the blade interaction frequency.

The analysis of secondary flow phenomena demands for good modelling accuracy, and this

suggested the use of a LES turbulence model. The simulation was unsteady and the time step used was proportional to the blade passage time: this is necessary to ensure that the unavoidable time-filtering (proportional to the time step) is sufficiently smaller than the blade interaction frequency.

### 3.1. “2-D LES” simulation

A 2-D simulation was performed to calibrate the code and to identify the minimum mesh refinement necessary to properly visualize the main features of the flow. Though it is theoretically incorrect to talk about “2-D secondary flows”, many interesting results observed in our 2-D flow fields seem to “extend” in the additional direction, because they were subsequently detected also in the 3-D results. This is, however, somewhat irrelevant from the designer’s point of view, because the entropy generation maps, which we claim ought to be the “objective functions” of the design procedure, are essentially three-dimensional in their features.

First of all, from a global point of view, and with reference to the Renau maps (Renau et al., 1967), the operating point of the stator is well inside the so-called “large transitor stall” zone (Figure 8).

Under these operating conditions, the stator attains its maximum pressure recovery, but the flow field is characterized by an unsteady separation of the boundary layers, alternatively on the pressure and suction sides. The vortices thus generated are convected downstream by the mean flow and new ones are generated with a periodicity of about  $100t$ , where  $t$  is the characteristic fluid residence time (radial length divided by average flow speed) in the stator.

Remarkably, our 2-D calculation was also able to capture this effect. The vortex behavior is clearly outlined on the velocity vectors fields at

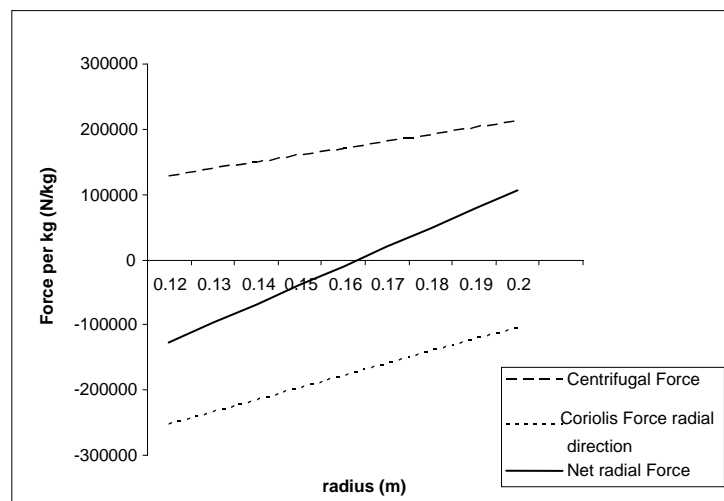


Figure 4. Magnitude of the mass forces in the radial direction.

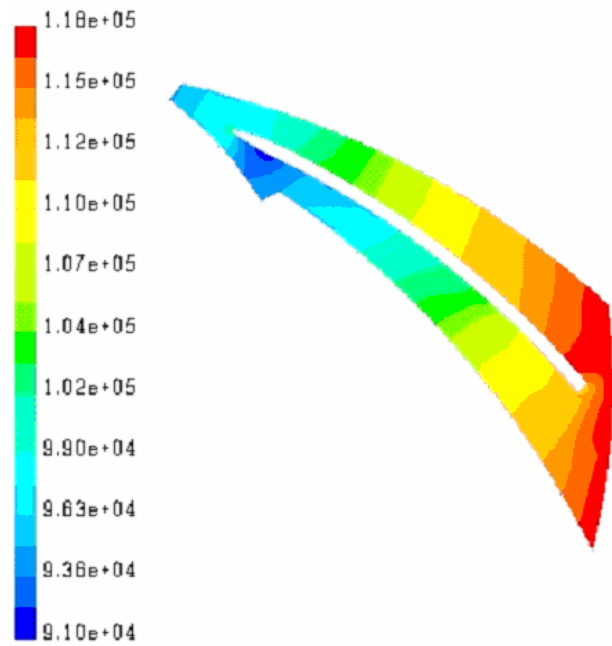


Figure 5. Static Pressure [Pa] Contours at mid span.

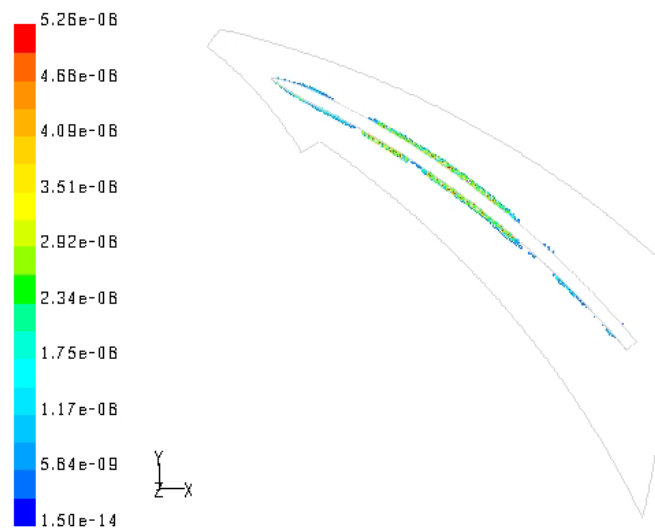


Figure 6. Thermal entropy generation rate [J/(kg K)] at mid span.

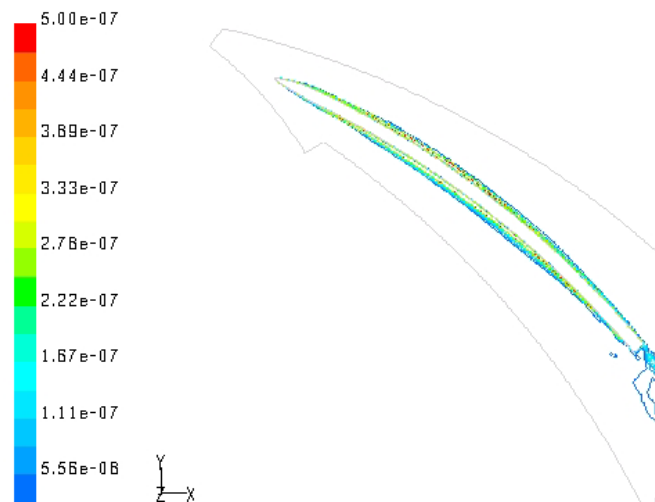


Figure 7. Viscous entropy generation rate [J/(kg K)] at mid span.

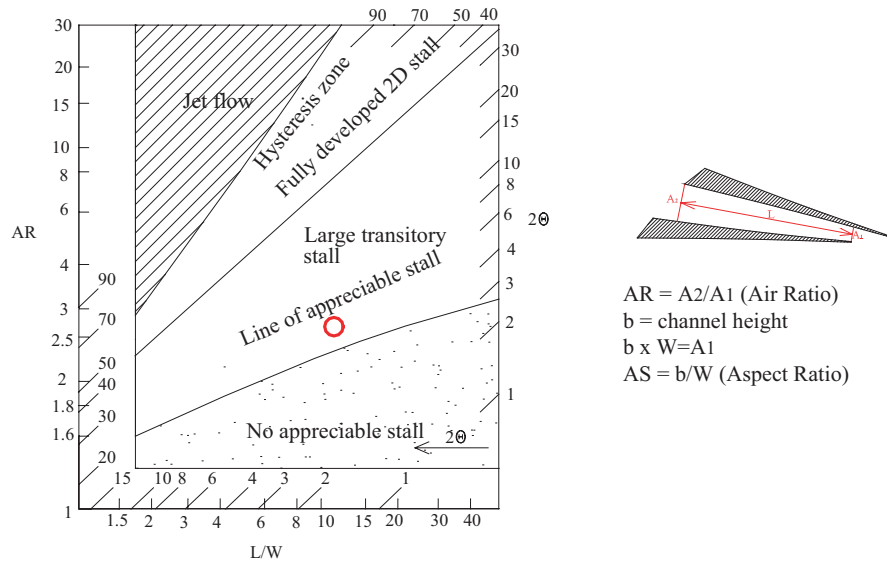


Figure 8. Renau Maps: The target symbol indicates the stator operating point.

TABLE III. – EFFECT OF THE MESH REFINEMENT ON THE ENTROPY GENERATION RATE

$y^+$	18	8	5	$(\text{value})_5/(\text{value})_{18}$	$(\text{value})_5/(\text{value})_8$
$\dot{s}_t$	0.000084	0.0017	0.0019	2.262	1.117
$\dot{s}_v$	0.0572	0.0877	0.1013	1.77	1.155
$\eta$	0.91	0.89	0.88	0.967	0.988

different time steps (Figure 9). Their dynamic description is not complete, because the 2-D simulation does not reveal the 3-D effect due to stretching and tilting, but the simulation allows a greater insight into the physics of the problem than originally expected.

The analysis of the entropy generation in the channel confirms that the main contribution is due to the viscous part, which is one order of magnitude greater than the thermal one (Figures 10 and 11)

From the time of evolution of the temperature field, it can be seen how the 2-D vortices convect the turbulent energy released from the boundary layer when it separates. This is represented by a peak of the advected temperature and can be physically interpreted as a transfer of energy due to coalescence from the smaller scales constituting the boundary layer to the larger scales of the vortices. For convenience, we have placed a movie of the time-history of vortex development on [www.turbomachinery.it](http://www.turbomachinery.it).

The sub-grid (SGS) turbulent kinetic energy is small in the entire flow field, which means that the grid is sufficiently accurate. An SGS peak is observed on the border between the vortex and the main flow, suggesting that in this zone smaller scales, not resolved by the grid, are generated (and convected as well).

The integral value of the local entropy generation rate demonstrates that the results are quantitatively correct. A mesh sensitivity analysis performed by reducing the  $y^+$  value at the wall shows, though, that a mesh refinement affects in non-negligible measure the global value of the entropy generation.

Three different mesh refinements have been tested, with a  $y^+$  value of 18, 8 and 5, respectively. It is expected that the larger the  $y^+$ , the smaller the accuracy on the boundary layer behavior. This will lead to an incorrect (underestimated) value of the entropy production rate and hence to an incorrect stator efficiency value. Table III shows the numerical results, confirming the sensitivity of the quantitative entropy production predictions to the boundary layer meshing.

As expected, both the thermal and the viscous contributions increase with improved boundary layer description accuracy, but the former is more deeply affected by a reduced amount of detail ( $\dot{s}_{t,5}/\dot{s}_{t,18} = 2.262$ ). Anyhow, even the efficiency calculated with the finest mesh (88%) is quite far from the real one, which is in the order of 75%. There are two main reasons for this. First, the vortex dissipation effect induced by their stretching in the axial direction cannot be taken into account in 2-D

(this is also a reminder that 2-D simulation cannot be used to study the entropy production of complex flows). Second, in 2-D simulations the dissipative effects due to the boundary layers on the hub and shroud walls are not simulated, and their entropy production is not taken into account.

The solution without pulsating boundary condition shows the wake vortex shedding, whose frequency is in the order of 300 Hz (Figure 9). The Strouhal number corresponding to this operating condition is equal to 0.1.

The 2-D solution outlines many interesting aspects of the main flow and allows for a rather accurate visualization of the effect of the secondary flows. But, even if there are analogies with the 3-D mid span flow, the 3-D vortex behavior is different and needs to be separately investigated, together with the effect of the other walls.

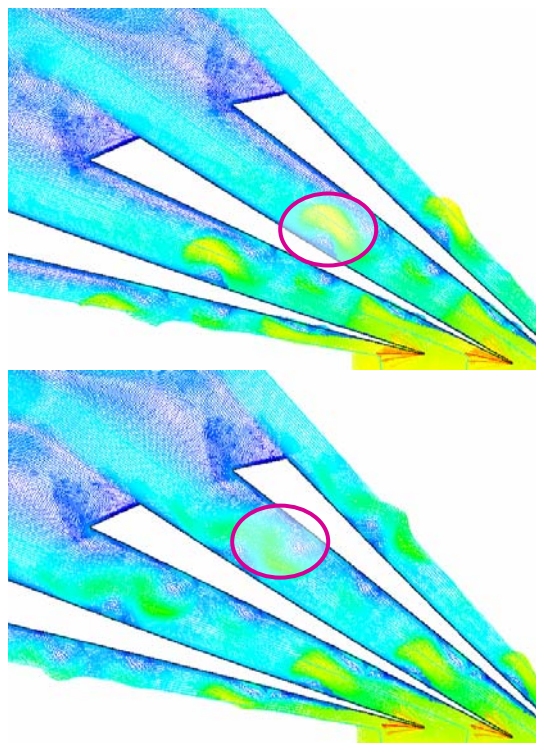


Figure 9. 2-D velocity vectors at  $t=4.09$  ms and  $t=6.03$  ms. The circled vortex is being convected downstream.

### 3.2. 3-D LES simulation

A 3-D simulation has been performed neglecting the axial effects induced by the rotor outflow (Cerini, 2001). The reason for this strong assumption is that the study was only intended to show how circumferential distortions in the rotor outflow influence the stator dynamics.

The air flows through the stator against a static pressure gradient, and energy must be transferred from the kinetic to the static pressure modes. When the compressor is operating in the

“large transitory stall” area of the Renau maps, the pressure counter-gradient is strong enough to reverse the flow direction in some regions of the passage, leading to the generation of large vortices that reduce the stage efficiency (Harada, 1988) by producing large amounts of viscous and thermal entropy (Sciubba, 2005).

The effect of the pressure countergradient is clearly captured by our 3-D calculation, which also shows a counter flow developing in the corner between the blade and the hub (Inoue and Cumpsty, 1984; Justen et al., 1999). The section of the channel spanned by this “blockage” is increasing towards the trailing edge, where the effect of the wake superimposes a swirling motion on it. This secondary motion is appreciable both on the pressure and (to a slightly smaller extent) on the suction sides of the stator (Figure 12).

There is no particular reason for the flow to display a preferential separation on the hub or on the shroud. In spite of the geometrical symmetry, an asymmetry is introduced when a disturbance on the hub side is created by the vortex generation process. The generated counterflow causes a dynamic asymmetry and pushes the main flow towards the opposite part of the channel. The free area available to the air passage is reduced by the presence of the recirculation region, and this leads to an undesired acceleration. On the other hand, this acceleration stabilizes the shroud boundary layer, thus reducing the possibility of flow separation on that side.

The accuracy of the numerical simulation was tested in accordance to the prevailing criteria (see Iandoli, 2000a,b). The consistency of the results with the scant available experimental data was verified by comparing global stage characteristics (see Iandoli, 2000a,b); Inoue and Cumpsty, 1984; Justen et al., 1999; Krain, 1981). Additionally, the results were compared with some published numerical studies (Casartelli et al., 1999; Dawes, 1995; Harada, 1988; Hathaway et al., 1992), and - once properly scaled - provided good agreement.

From a fluid dynamic point of view, the pressure recovery is extremely steep in the first unvaned portion of the stator, upstream of its leading edge. This is in part due to the blockage induced by the blade stagnation point and in part to the suddenly increasing passage area. The resulting large pressure gradient negatively affects the efficiency and promotes the generation of thermal entropy. The blade shape (that creates a channel with a divergence angle of  $7^\circ$ ) provides instead a smooth increase of the channel cross-sectional area (entropy generation is lower here).

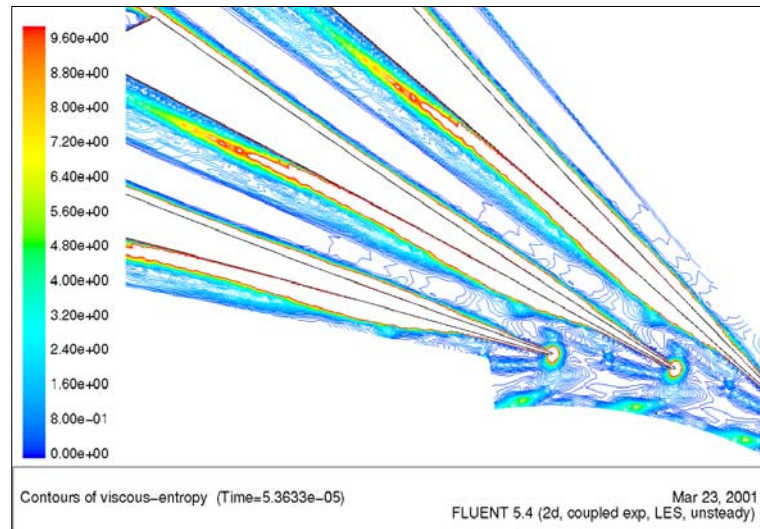


Figure 10. Viscous entropy generation rate contours.

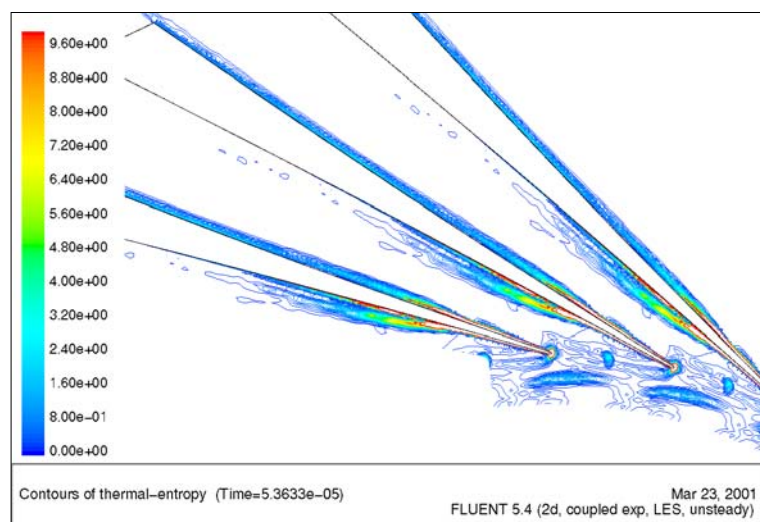


Figure 11. Thermal entropy generation rate contours.

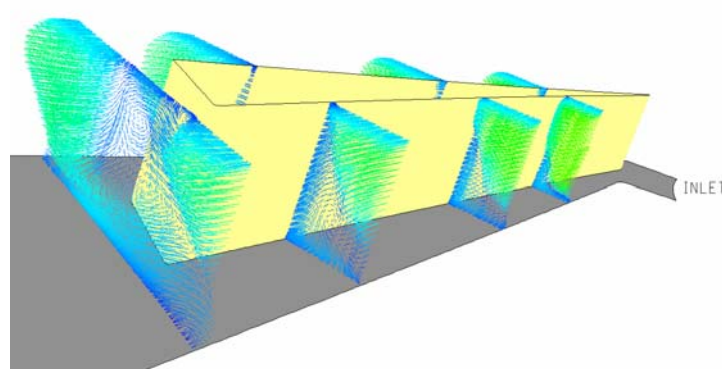


Figure 12. The development of the counter vortex.

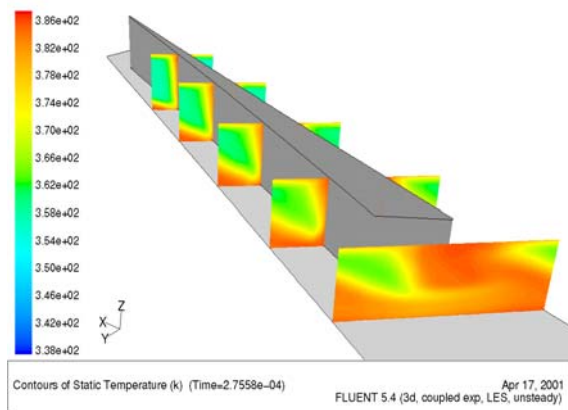


Figure 13. Temperature contours.

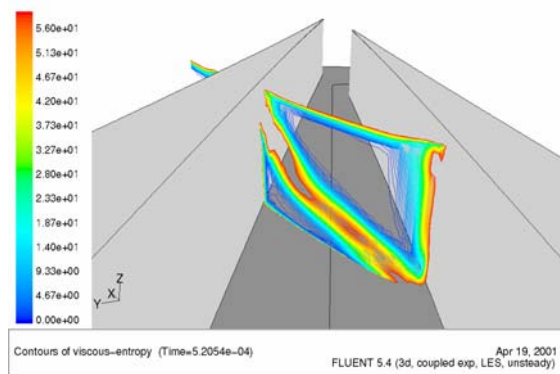


Figure 14. Velocity contour in the stator.

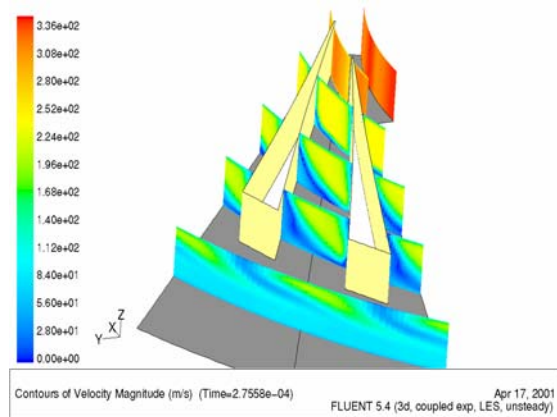


Figure 15. Viscous entropy generation contours.

Downstream of the leading edge, acceleration is observed while the flow crosses the throat section. This can be explained by observing that just upstream of the leading edge the local  $Ma$  is 0.88, and the flow becomes locally transonic in the proximity of the blade, giving origin again to an area of relatively high entropy generation.

Within the channel, the expansion is smooth as expected, but the pressure gradient almost disappears near the trailing edge,

suggesting that the present stator might have been “overdesigned” as far as its radial length is concerned.

Effects due to the counterflow become evident if one looks at the temperature field (Figure 13). In the recirculation region, the temperature increases because of strong deceleration and viscous-to-thermal dissipation, until it reaches the total temperature value observed at the stagnation point. This effect is detectable in the velocity field that shows a counterflow velocity as high as 50 m/s (Figure 14). Likewise, the temperature and pressure fields show the fully 3-D nature of the flow. While the pressure field does not change substantially from root to tip, both the temperature and the velocity do. This affects the entropy generation rate and explains why the 2-D integral value was underestimated.

The contours of both the thermal (not reported) and viscous (Figure 15) entropy generation rates show that, contrary to the 2-D case, the production is not limited within the boundary layers, but a substantial part of entropy is generated in the middle of the channel by the strong velocity and pressure gradients. This is not surprising, since the velocity defect between the main and the counter flow is close in absolute value to the velocity of the main flow relative to the walls (Figure 14). Both viscous and thermal entropy generations are confined to the walls until the separation point is reached, confirming that the main flow is substantially inviscid, as also shown by the vorticity contours: after the separation point, the viscous nature of the flow becomes dominant and the entropy generation rate is of the same order of magnitude as that in the boundary layers.

The stator efficiency computed by integrating the local entropy generation rates gives a value of 75%, in very good agreement with the real one. This efficiency is calculated as (Bejan, 1982):

$$\eta_s = \frac{1}{1 + \frac{2T_0\Delta S}{\dot{m}V_{2r}^2}} = 75\% \quad (6)$$

The computed isentropic efficiency of the entire stage is 0.7, very close to the value provided by the manufacturer.

#### 4. Conclusions

The entropy generation approach used in this work proved its capacity to provide the designer with useful details about the flow field. Nevertheless, the simulation must be carried out keeping in mind that great detail is necessary to obtain quantitative results. In this case, as in all radial compressors, the complex 3-D flow

phenomenology inhibits the use of a 2-D approach, in which only the pressure behavior could be reasonably resolved. The calculation of the entropy generation rates requires a quite fine mesh in the proximity of the walls: in the present case, a value of  $y^+ > 8$  was yet insufficiently accurate.

The adverse pressure gradient induces a counter flow, as confirmed by some of the numerical works available in the literature, and the sonic effects in the throat region affect the pressure recovery by introducing a local expansion. Both of these effects are detected by the entropy generation rate maps, which record a substantial increase of the viscous component  $s_v$ . The unsteady incoming flow is not smoothed within the annulus (where the entropy production remains relatively low): a remarkable portion of the pressure variations reaches the blade and is attenuated only after about the channel mid-length: again, in this area of pressure recovery, both the thermal and the viscous entropy generation present higher values (the thermal contribution being substantially smaller because it is given only by viscous heating effects). On the other hand, the pressure recovery is not substantially modified by the recirculation whose phenomenology is accurately reproduced by the LES model. The unsteady stall in the diffuser is also detectable in terms of entropy generation because its “trace” is a high entropy wake that is convected away from the diffuser.

Finally, for more detailed information and color versions of a number of the figures presented in this paper, the reader is referred to [www.turbomachinery.it](http://www.turbomachinery.it).

### Acknowledgements

All simulations described in this paper were performed on a cluster of workstations at the ENEA (Italian Agency for Alternative Energy) facilities in the Frascati Research Center, near Rome. The CFD code was FLUENT-5.4™, and its mesh generator, GAMBIT™.

### Nomenclature

$C_p$	Pressure Recovery Coefficient
$C_{p,tot}$	Total Pressure Loss Coefficient
$\Delta S$	Global Entropy Production Rate [W/K]
$m$	Mass Flow Rate [kg/s]
$Ma$	Mach Number
$p_1$	Static Pressure at Rotor Inlet [Pa]
$p_2$	Static Pressure at Rotor Outlet [Pa]
$p_4$	Static Pressure at Stator Outlet [Pa]
$p_{tot}$	Total Pressure [Pa]
$\dot{s}_t$	Thermal Entropy Production Rate [J/(kg*K)]
$\dot{s}_v$	Viscous Entropy Production Rate [J/(kg*K)]

$T$	Static Temperature [K]
$T_{tot}$	Total Temperature [K]
$T_0$	Reference Temperature [K]
$V_{2r}$	Absolute Radial Velocity at Rotor Outlet [m/s]
$\beta_{stage}$	Stage Pressure Ratio
$\eta_{pol}$	Polytropic Efficiency
$\eta$	Stage Efficiency
$\eta_s$	Stator Efficiency
$\omega$	Angular Velocity [rad/s]

### References

- Bejan A.: *Entropy generation through heat and fluid flow*. New York: J. Wiley & Sons, 1982.
- Casartelli E., Saxer A.P., Gyarmarthy, G.: *Numerical Flow Analysis in a Subsonic Vaned Radial Diffuser with Leading Edge Redesign*. J. Turbom. 1999 (1); Vol. 121.
- Cerini R.: *Application of an LES turbulence model on the simulation 2-D and 3-D of a Vaned Radial Diffuser*. M.E. Thesis, U. Rome 1, 2001 (in Italian).
- Dawes W. N.: *A Simulation of the Unsteady Interaction of a Centrifugal Compressor with Its Vaned Diffuser*, J. Turbom. 1995 (4); Vol.107.
- Harada H.: *Performance Characteristics of Two- and Three-Dimensional Impellers in Centrifugal Compressors*. J. Turbom. 1988(1); Vol.110.
- Hathaway M.D., Chriss M.R., Wood J.R., Strazisar A.J.: *A NASA Low-Speed Centrifugal Compressor for Three-Dimensional Viscous Code Assessment and Fundamental Flow Physics Research*. J. Turbom. 1992 (4); Vol.114.
- Iandoli C. L.: *Analysis of the entropy generation fields of a low  $n_s$  centrifugal compressor*. M.E. Thesis, U. of Roma 1, 2000a (in Italian).
- Iandoli C. L., Sciubba E.: *Entropy generation maps of a low-specific speed radial compressor rotor*. Proc. AES/ASME W. Meeting, Orlando, FL, USA, 2000b.
- Inoue M, Cumpsty N. A.: *Experimental Study of Centrifugal Impeller Discharge Flow in Vaneless and Vaned Diffusers*. J. Eng. G.T. & Power 1984 (4); Vol.106.
- Justen F., Ziegler K.U., Gallus H.E.: *Experimental Investigation of Unsteady Flow Phenomena in a Centrifugal Compressor Vaned Diffuser of Variable Geometry*. J. Turbom. 1999 (10); Vol. 121.
- Krain H.: *A Study on Centrifugal Impeller and Diffuser Flow*. J. Turbom. 1981 (10); Vol.103.
- Krain H.: *Swirling Impeller Flow*. J. Turbom. 1988 (1); Vol.110.
- Natalini G, Sciubba E.: *Minimisation of the local rates of entropy production in the design of air-cooled gas turbine blades*. J. Eng. G.T. & Power 1999 (7); Vol. 121(3).

Peeters M, Sleiman M.: *A Numerical Investigation of the Unsteady Flow in Centrifugal Stages*. ASME 2000-GT-426, May 2000.

Renau L.R., Johnston J.P., Kline S.J.: *Performance and Design of Straight Two-Dimensional Diffusers*. J. Basic Eng., v. 89, 1967.

Sciubba E.: *Entropy production rates as a true measure of viscous and thermal losses in thermo-mechanical components*. NATO-W.shop on Heat- & Mass Transfer, Bucharest, 1994.

Sciubba E.: *Computing the entropy generation rate for turbomachinery design applications: can*

*a diagnostic tool become a predictive one?* To appear 2005.

Shum Y. K. P., Cumpsty N. A.: *Impeller-Diffuser Interaction in Centrifugal Compressor*. ASME 2000-GT-428, May 2000.

Stein W, Rautenberg M.: *Analysis of Measurements in Vaned Diffusers of Centrifugal Compressors*. J. Turbom. 1988 (1); Vol.110.

Umlauf L., Burchard H.: *Second-order turbulence closure models for geophysical boundary layers. A review of recent work*. Continental Shelf Research, Volume 25: 795-827, Issue 7-8, May 2005.